Theory of Strain Phase Equilibria and Diagrams

Bo Wang^{1,2,*} and Long-Qing Chen^{1,*}

Abstract

Chemical phase equilibria and phase diagrams are well established and have served as indispensable guides for designing materials through chemical tuning. However, a general thermodynamic theory for strain phase equilibria remains elusive despite extensive studies which have revealed dramatic impacts of mechanical strain on the stability of phases and domain states in solid-state materials. Here, we establish the thermodynamic theory of strain equilibria and a general framework for efficiently constructing multidomain and multiphase diagrams of arbitrarily strained solids under incoherent conditions. As examples, we obtain temperature-strain phase diagrams of ferroelectric PbTiO₃, strongly correlated VO₂, and unconventional ferroelectric Hf_{0.5}Zr_{0.5}O₂. We reveal the analogs of the Gibbs phase rules, multiple- and multi-critical points, common-tangent construction, and level rule in strain equilibria to those in the familiar chemical phase equilibria. Our strain equilibria theory offers a powerful framework for predicting the thermodynamic stability of structural phases and domains in strained solids and for guiding the strain engineering of their functional properties.

Keywords

Thermodynamics, solid state phase transformation, phase diagram, ferroelectric, stress and strain

¹Materials Research Institute and Department of Materials Science and Engineering, The Pennsylvania State University, University Park, PA 16802, USA

²Materials Science Division, Lawrence Livermore National Laboratory, Livermore, CA 94550, USA

^{*}Corresponding authors: wang111@llnl.gov (B.W.) and lqc3@psu.edu (L.-Q. C.)

1. Introduction

Phase diagrams of materials generally refer to the graphical representation of phase equilibria as a function of temperature, pressure, and chemical composition and have been one of the most utilized guides for the design and processing of materials. Over the past two decades, driven by continuing miniaturization of electronic devices, extensive studies have demonstrated the profound effects of strains on the stability of solid-state phases and domain variants, particularly for crystalline materials at small length scales that can withstand much larger strains than their bulk counterparts¹. Strain has now become an important thermodynamic variable besides chemical composition that can be utilized to tune not only the lattice parameters and crystallographic symmetry, but also the electronic structures, mesoscale microstructures, and phase transition behaviors of various materials to drastically enhance their macroscopic functional properties, leading to the establishment of a major branch of materials research, strain engineering¹. Examples of strain engineering include tuning band structures of semiconductors², enhancing ferroelectricity³, stabilizing hidden topological phases⁴, unlocking otherwise forbidden magnetic switching⁵, and modulating phase transition in strongly correlated electronic materials⁶

Strain can be represented by a symmetric second-rank tensor comprising of six independent components. Therefore, the design space for a strained single-component solid contains seven independent variables¹. To guide the rational exploration of such high-dimensional space, it is of critical importance to establish the general thermodynamic principles to efficiently construct the temperature-strain phase diagrams which graphically represent the thermodynamic equilibrium states of a solid as a function of strain and temperature. Despite that the thermodynamics of multicomponent solids subject to nonhydrostatic stress have been established¹⁰, they were mostly used for understanding the mechanical effects on the chemical phase equilibria in chemically inhomogeneous systems. However, many applications of strain engineering refer to chemically homogeneous, yet structurally inhomogeneous systems subject to anisotropic mechanical boundary conditions with mixed strain and stress components. Existing theoretical efforts in this vein have been predominantly focused on ferroic epitaxial thin films based on either *a priori* assumptions on possible multi-phase/multi-domain configurations^{11,12} or monodomain states¹³. Alternatively, the employment of expensive first-principles calculation-based methods¹⁴⁻¹⁶ and

phase-field simulations¹⁷, though free of *a priori* assumptions on the domain states, are generally limited to creating two-dimensional strain phase diagrams that correspond to, e.g., epitaxial thin films subject to anisotropic biaxial clamping. These computational methods are computationally expensive and are thus generally inefficient for constructing high-dimensional strain phase diagrams for materials subject to extraordinarily large strains¹⁸ or more complex deformation modes^{19,20}, such as twisting²¹, bending^{22,23}, and folding²⁴. Therefore, it is of broad interest to develop a general, yet easy to implement, thermodynamic theory to predict the phase equilibria of strained solids in the high-dimensional temperature-strain space.

In this work, we establish a general thermodynamic theory of incoherent strain phase equilibria which can be employed to efficiently construct multi-phase/multi-domain strain phase diagrams of arbitrary solids. It should be emphasized that essentially almost all existing temperature-composition phase diagrams are incoherent phase diagrams, and yet they provide useful guidance to materials design, experimental synthesis, and characterization. We demonstrate the applicability of our theory by establishing the strain and stress phase diagrams of distinct material systems, including the classical ferroelectric PbTiO₃, strongly correlated VO₂ undergoing both electronic and structural phase transitions, and unconventional ferroelectric Hf_{0.5}Zr_{0.5}O₂ thin films exhibiting rich polymorphism. We present the generalized Gibbs phase rules, multiple-points and multi-critical points, common-tangent construction, and the level rule for evaluating the coexisting phases/domains fractions, by drawing analogous to the chemical equilibria and temperature-composition phase diagrams of multicomponent systems. Extension of the present method to account for the coherent strain/stress effect on the strain phase equilibria and diagrams is briefly discussed.

2. Theory

Strain and stress can be regarded as mechanical analogs of the chemical composition and chemical potential as a conjugate pair of thermodynamic state variables^{25,26}. For a closed system subject to mechanical deformation, the differential form of the fundamental equation of thermodynamics in terms of the Helmholtz free energy density $f(T, \varepsilon_i)$ can be written as

$$df = -sdT + \sum_{i=1}^{6} \sigma_i d\varepsilon_i, \tag{1}$$

where T and s are respectively the temperature and entropy density, and σ_i and ε_i are respectively the stress and strain in Voigt notation. The corresponding differential form for the Gibbs free energy density reads as

$$dg = -sdT - \sum_{i=1}^{6} \varepsilon_i d\sigma_i. \tag{2}$$

Equation (1) or (2) represents a convenient differential form of the fundamental equation of a solid subject to strain or stress, respectively. Note that all the volume density quantities (such as f, g, s, and ε_i) are measured with respect to the same reference state.

If a solid is subject to a combination of strain and stress, we can define a family of modified Helmholtz free energy densities at a constant temperature with mixed strain and stress components as independent variables,

$$f_{\{e\}}^{\{s\}} \left(\sigma_{i,i \in \{s\}}, \varepsilon_{i,i \in \{e\}} \right) = f - \sum_{i \in \{s\}} \sigma_i \varepsilon_i, \tag{3}$$

where $\sigma_{i,i\in\{s\}}$ and $\varepsilon_{i,i\in\{e\}}$ are the independent or natural variables of $f_{\{e\}}^{\{s\}}$, the sets $\{s\}$ and $\{e\}$ list the indices of the corresponding stress and strain variables, and thus $\{s\} \cup \{e\} = \{1,2,3,4,5,6\}$. Alternatively, one can also define the modified Gibbs free energy density $g_{\{s\}}^{\{e\}}$, which is equivalent to $f_{\{e\}}^{\{s\}}$ (See **Supplementary Note 1**).

We now discuss the strain phase equilibria and diagram of a single-strain-component system and then extend it to multi-strain-component systems. Consider a solid at a constant temperature consisting of two possible chemically identical but structurally different phases α and β (which termed as strain phases or strain domains if they share the same symmetry). Suppose that the strain component ε_1 of the two-phase or two-domain solid is subject to an external constraint while the other non-conjugate stress components of both phases or domains are unchanged, i.e., $d\sigma_i = 0$ (i = 2, ..., 6). This scenario may correspond to a uniaxially strained nanorod between the two phases. Equation 1 is reduced to

$$df_1 = \sigma_1 d\varepsilon_1. \tag{4}$$

Depending on the value of ε_1 , the equilibrium state can be a single α -phase/domain, a single β -phase/domain, or a mixture of the two. The free energy density as a function of the strain ε_1 for each phase, $f_1^{\alpha}(\varepsilon_1^{\alpha})$ and $f_1^{\beta}(\varepsilon_1^{\beta})$, can be obtained by integrating Equation (4) with a known strain-

stress relationship which can be acquired by phenomenological models, *ab initio* calculations, or experimental measurements (See **Supplementary Note 2 and Fig. S1** for detailed discussion).

Assuming the interface between α and β is incoherent with negligible interfacial energy, we can define the total free energy density of the two-phase mixture as $f_1^{\text{mix}}(\varepsilon_1) = \omega_{\alpha} f_1^{\alpha}(\varepsilon_1^{\alpha}) + \omega_{\beta} f_1^{\alpha}(\varepsilon_1^{\beta})$ where ω_{α} and ω_{β} are the corresponding volume fractions. The mechanical equilibrium of the system is achieved when $f_1^{\text{mix}}(\varepsilon_1)$ is minimized with respect to ω_{α} , ω_{β} , ε_1^{α} and ε_1^{β} subject to the constraints $\varepsilon_1 = \omega_{\alpha} \varepsilon_1^{\alpha} + \omega_{\beta} \varepsilon_1^{\beta}$ and $\omega_{\alpha} + \omega_{\beta} = 1$. This optimization problem corresponds to the common tangent construction of the convex hull of the two energy surfaces f_1^{α} and f_1^{β} , as shown in Fig. 1A, which is in analogous to identifying the incoherent chemical phase equilibria of a binary system²⁷. The common tangent line in the two-phase region requires that,

$$\frac{\partial f_1^{\alpha}}{\partial \varepsilon_1^{\alpha}}\Big|_{\varepsilon_1^{\alpha} = \varepsilon_1^{0,\alpha}} = \frac{\partial f_1^{\beta}}{\partial \varepsilon_1^{\beta}}\Big|_{\varepsilon_1^{\beta} = \varepsilon_1^{0,\beta}} = \frac{f_1^{\alpha}(\varepsilon_1^{0,\alpha}) - f_1^{\beta}(\varepsilon_1^{0,\beta})}{\varepsilon_1^{0,\alpha} - \varepsilon_1^{0,\beta}}, \tag{5}$$

where $\varepsilon_1^{0,\alpha}$ and $\varepsilon_1^{0,\beta}$ are the strains at the two tangent points corresponding to the local strains of each phase at equilibrium. When the applied strain falls in between $\varepsilon_1^{0,\alpha}$ and $\varepsilon_1^{0,\beta}$, a mixture of α and β has lower free energy than the single α - or β -phases, which defines the two-phase region of the single-component strain phase diagram.

Alternatively, we can establish the stress phase diagram for the two-phase system from the Gibbs free energy densities $g^{\alpha}(\sigma_1)$ and $g^{\beta}(\sigma_1)$ by Legendre transforming $f_1^{\alpha}(\varepsilon_1^{\alpha})$ and $f_1^{\beta}(\varepsilon_1^{\beta})$ with respect to ε_1^{α} and ε_1^{β} , respectively. The mechanical equilibrium between α and β is achieved when

$$\sigma_1^{\alpha} = \sigma_1^{\beta} = \sigma_1^0, \tag{6a}$$

$$g^{\alpha}(\sigma_1^{\alpha}) = g^{\beta}(\sigma_1^{\beta}) = g^0. \tag{6b}$$

This condition corresponds to the point of intersection of the two Gibbs free energy density curves in Fig. 1B. When $\sigma_1 < \sigma_1^0$, a single α -phase is more stable than a single β -phase, and when $\sigma_1 > \sigma_1^0$, a single β -phase is more stable. The corresponding single-component stress phase diagram

can be obtained by projection onto the stress axis. Note that Equation (6) also implies uniform chemical potential.

We observe that the equilibrium conditions in Equation (5) and (6) are equivalent which can be interpreted from Fig. 1 A and B. Specifically, the slope and y-intercept of the common tangent line in Fig. 1A equals respectively to the stress σ_1^0 and the Gibbs free energy density g^0 at the intersection point of g^{α} and g^{β} in Fig. 1B. The slopes and y-intercepts of the two tangent lines at the intersection point of g^{α} and g^{β} in Fig. 1B equal respectively to the local strains, $\varepsilon_1^{0,\alpha}$ and $\varepsilon_1^{0,\beta}$, and the associated Helmholtz free energy densities, $f_1^{0,\alpha}$ and $f_1^{0,\beta}$, at the two tangent points on the common tangent line in Fig. 1A, respectively. These corresponding relations also manifest themselves in the strain and stress phase diagrams, i.e., a two-phase region in the single-component stress phase diagram (a single point) corresponds to a two-phase region in the single-component strain phase diagram (a line segment). Similar corresponding relations exist for higher dimensional strain/stress phase diagrams as will be shown in the following.

We now generalize strain phase equilibria into two-strain- and multi-strain-component systems. For a two-strain-component system at a fixed temperature, the maximum number of possible coexisting phases is three following the generalized Gibbs phase rule^{28,29}. We label the three possible phases as α , β , and γ with homogeneous strains, ε_1^X and ε_2^X ($X = \alpha$, β , γ) at equilibrium, while all other independent stress components are fixed, i.e., $d\sigma_i^X = 0$ (i = 3,4,5,6, X= α , β , γ). The triangular region of the common tangent plane of $f_{1,2}^X$ ($X = \alpha$, β , γ) bounded by the three tangent points corresponds to the three-phase coexisting region in the ε_1 - ε_2 diagram (shaded region in Fig. 1C). For each two of $f_{1,2}^X$ ($X = \alpha, \beta, \gamma$), we can identify a set of common tangent planes and the associated tangent points and lines (thin black segments in Fig. 1C). These lines link the local strains at equilibrium and constitute the two-phase regions in the ε_1 - ε_2 phase diagram, as analogs of the tie-lines in chemical phase diagrams²⁷. We can also establish the two-component stress phase diagram by equating the Gibbs free energy densities, $g^X(X = \alpha, \beta, \gamma)$, as shown in Fig. 1D. The intersection curves between each two g^X surfaces correspond to the equilibrium of the two phases. The three curves intersect at a point where the three phases coexist, i.e., the triple point. The two-component stress phase diagram can be obtained by projecting the two-phase curves and the triple point onto the σ_1 - σ_2 plane. The resulting σ_1 - σ_2 phase diagram consists of three single-phase regions, three two-phase regions, and one triple point. The generalized Gibbs phase

rule^{28,30} can be utilized to calculate the degree of freedom (DOF) of each phase region. For example, in any two-phase boundary of Fig. 1D, the DOF is calculated as $n_s - n_p + 1 = 2 - 2 + 1 = 1$, where n_s is the number of fixed stress components and n_p is the number of coexisting phases/domains. The fact that DOF = 1 suggests that σ_1 and σ_2 cannot vary independently without breaking the two-phase equilibria. Comparing Fig. 1C and 1D, we observe that: (1) the triple point in the σ_1 - σ_2 phase diagram corresponds to the three-phase triangle in the ε_1 - ε_2 phase diagram; (2) the two-phase boundaries in the σ_1 - σ_2 phase diagram correspond to the two-phase regions in the ε_1 - ε_2 phase diagram; (3) each point on the two-phase boundaries in the σ_1 - σ_2 phase diagram expands into a tie-line in the ε_1 - ε_2 phase diagram.

For three-strain-component systems at a fixed temperature, the maximal number of coexisting strain phases/domains is four, labled as α , β , γ , and δ . It is challenging to visualize the free energy hypersurfaces of $f_{1,2,3}^X$ and $g^X(X=\alpha,\beta,\gamma,\delta)$ in three dimensions, but we can envision the corresponding three-component strain and stress phase diagrams by generalizing the singlecomponent and two-component cases, as illustrated in Fig. 1E and F, respectively. By employing the generalized Gibbs phase rule, we can validate that Fig. 1F consists of one quadruple point with DOF = 0, four three-phase curves with DOF = 1, six two-phase surfaces with DOF = 2, and four single-phase volumetric regions DOF = 3. The corresponding strain phase diagram (Fig. 1E) can be rationalized by identifying the corresponding relations with respect to Fig. 1F. Specifically, Fig. 1E consists of: (1) one tetrahedral four-phase region corresponding to the quadruple point in Fig. 1F; (2) four triangular-prismatic three-phase regions extruding from each face of the tetrahedron, corresponding to the four triple-lines in Fig. 1F; (3) six triangular-prismatic two-phase regions sharing one edge with the tetrahedron, corresponding to the six two-phase planes in Fig. 1F; (4) four pyramidal single-phase regions sharing one vortex with the tetrahedron, corresponding to the four volumetric single-phase regions in Fig. 1F. Notably, the phase regions of a three-component strain phase diagram of realistic materials may be distorted polyhedra with curved edges and faces. Nevertheless, their topology should remain invariant and satisfies the Euler characteristics for 3-D convex polyhedra³⁰.

In principle, the generalized Gibbs phase rule, the corresponding relationship between stress and strain phase diagrams, and the topological characteristics of the phase regions apply to strain phase diagrams with an arbitrary number of strain components. We summarize several generalized features and rules for *n*-dimensional strain/stress phase diagrams in Table 1. In addition, we provide schematics of three typical chemical phase diagrams in Fig. 1G-I to reveal the analogy between strain phase equilibria and chemical phase equilibria.

3. Results

To demonstrate practical application of the incoherent strain phase equilibria theory, we establish the temperature-strain/stress phase diagrams for three solid-state materials undergoing structural phase transitions driven by distinct physics. Detailed description of the physical models for each material is given in **Supplementary Note 3**.

3.1. Biaxially strained PbTiO₃

PbTiO₃ is a classical ferroelectric material undergoing a displacive phase transition from a nonpolar cubic phase (Pm $\overline{3}$ m) to a tetragonal polar phase (P4mm) at the Curie temperature $T_{\rm C} \sim 756$ K in the stress-free bulk state at ambient pressure. The development of spontaneous polarization in the polar phase results in three energetically degenerate tetragonal domain states. For (001)-oriented PbTiO₃ epitaxial thin films subject to biaxial strains, the three ferroelastic domain variants are often labeled as a_1 -, a_2 -, and c-phases.

We establish the σ_1 - σ_2 phase diagrams of PbTiO₃ at T=300 K from the equilibrium Gibbs free energy densities g of the a_1 -, a_2 -, and c-phases, and then apply the Legendre transform to obtain the corresponding ε_1 - σ_2 , σ_1 - ε_2 , and ε_1 - ε_2 phase diagrams (Fig. 2). The phase regions in each diagram are correlated as indicated by the dashed lines. By varying the temperature, we obtain a set of isothermal σ_1 - σ_2 and ε_1 - ε_2 phase diagrams to establish the T- σ_1 - σ_2 phase and T- ε_1 - ε_2 phase diagrams for biaxially constrained PbTiO₃ (Fig. 3A,B). When $T < T_C$, the isothermal ε_1 - ε_2 and σ_1 - σ_2 phase diagrams are isomorphic to Fig. 2B and C. When $T > T_C$, the paraelectric (PE) phase emerges as a stable phase at small strain/stress states along with three triple points referring to the coexistence between the PE phase and each two of the a_1 -, a_2 -, and c-phases (Fig. 3C,D). We observe several corresponding relations between the T- ε_1 - ε_2 and T- σ_1 - σ_2 phase diagrams, e.g., each point on the four three-phase lines in Fig. 3A expands into a three-phase triangle in Fig. 3B; the stacking of these four sets of triangles constitutes four prismatic three-phase regions; the four prismatic regions meet at a triangle in the horizontal plane at $T = T_C$ which represents the four phase equilibria. Notably, Fig. 3A is a direct realization of Fig. 1E while Fig. 3B become

isomorphic to Fig. 1F by Legendre transforming the temperature into the entropy density (Supplementary Fig. S2).

We can further obtain the T- σ and T- ε phase diagrams of PbTiO₃ subject to equi-biaxial stress or strain (Fig. 3E and F) with $\sigma = \sigma_1 = \sigma_2$ and $\varepsilon = \varepsilon_1 = \varepsilon_2$ by cross-sectioning Fig. 3A and B, respectively. Under an equi-biaxial strain/stress, the a_1 - and a_2 -phases are degenerate, and the resulting T- ε phase resembles the temperature-composition phase diagram of a binary solution with an eutectic reaction²⁷. Just as their chemical counterparts, the eutectic-like reaction in the strain phase equilibria in Fig. 3B, i.e., PE phase $\rightarrow c$ -phase + a_1/a_2 -phase, may lead to the formation of unique microstructures, e.g., superdomain structures in PbTiO₃-based thin films³¹.

Notably, Fig. 3F suggests that the ferroelectric and paraelectric phases coexist for biaxially strained PbTiO₃ for both the compressive and tensile strain states. In contrast, almost all existing *T-\varepsilon* phase diagrams of PbTiO₃ films^{11,13} indicate continuous phase transitions between the ferroelectric and paraelectric phases under biaxial strains. Such a discrepancy is related to the controversy on the nature of structural phase transformation in inhomogeneous systems^{12,32–34}. It is argued that the first-order transition of a stress-free ferroelectric becomes second order in the strained case only if the system remains homogeneous; otherwise, an inhomogeneous two-phase state is energetically favored within a finite temperature interval^{32,34}. Here, we demonstrate that, under the incoherent strain assumption, the ferroelectric-to-paraelectric transition in biaxially strained PbTiO₃ is of first order regardless of the type of the biaxial strains. Nevertheless, it remains an open question whether this two-phase coexistence can be observed in experiments because the presence of interfaces (including the heterophase boundaries, surfaces, film-substrate interfaces, and domain walls) and electrostatic energy contributions, which are not considered in the present strain phase equilibria analyses, may alter the behavior of the phase transition³⁴.

3.2. Uniaxially strained VO₂

Bulk VO₂ is a strongly electron-correlated material undergoing a hallmark metal-to-insulator transition upon cooling from a metallic rutile phase (R phase) to an insulating monoclinic M1 phase at $T_{\rm C} \sim 340$ K, which is promising for neuromorphic computing³⁵. For VO₂ nanowires subject to uniaxial stretching, another insulating monoclinic M2 phase can be induced, which coexists with the M1 and R phases at a triple point at the temperature $T_{\rm tri}$ 9. Using the

thermodynamic free energy of VO₂ from Ref. ³⁶, we reproduced the temperature-stress phase diagram of VO₂ subject to uniaxial stress along the c-axis of the R phase in Fig. 4A, which agrees well with the experimental measurements. We convert Fig. 4A into the $\varepsilon_{33} - T$ phase diagram by performing Legendre transform (Fig. 4B), which can be used to guide experiments in determining the critical applied strain to induce the metal-to-insulator transition in VO₂ nanowires⁹. Although uniaxial strain is considered here for simplicity, the same procedure is applicable to establishing the multiphase/multidomain phase diagrams of VO₂ for arbitrary strain and stress states, which can be remarkably useful for understanding the coupled structural and electronic phase transitions in VO₂ subject to more complex modes of deformations.

3.3. Uniaxially strained Hf_{0.5}Zr_{0.5}O₂

HfO₂-based ferroelectric thin films have gained surging research interest because of the unconventionally robust ferroelectricity down to the nanoscale and compatibility with the established semiconductor industry³⁷. The ferroelectricity in Hf_{0.5}Zr_{0.5}O₂ thin films has been ascribed to the stabilization of an orthorhombic polar phase (Pca2₁) which is otherwise metastable/unstable in bulk crystals³⁷. Therefore, it is of critical importance to identify the key factors that stabilize the polar phase in Hf_{0.5}Zr_{0.5}O₂ thin films. However, the complex polymorphism³⁸ of Hf_{0.5}Zr_{0.5}O₂ makes it a non-trivial task to identify the necessary order parameters to describe the structural phase transformations and the associated ferroelectric transitions. Nevertheless, we show that the strain phase diagram of Hf_{0.5}Zr_{0.5}O₂ can be conveniently established using the strain phase equilibria theory with a minimal set of input parameters computable from first-principles calculations. For simplicity, we consider Hf_{0.5}Zr_{0.5}O₂ thin films subject to one-component normal strain ε_1 and four possible polymorphic phases of Hf_{0.5}Zr_{0.5}O₂ with (001) orientation, including the tetragonal P4₂nmc phase (T phase), monoclinic P2₁/c phase (M phase), orthorhombic Pca2₁ polar phase (O phase), and cubic Fm3m phase (C phase). The elastic, surface, and bulk energy contributions of each phase are included in the Helmholtz free energy density. All model parameters are adopted from first-principles-based calculations in literature^{38,39}.

We obtain the T- σ_1 and T- ε_1 phase diagrams of a 20 nm Hf_{0.5}Zr_{0.5}O₂ thin film subject to one-component stress and strain in Fig. 4C and D, respectively. The stress phase diagram shows that the C phase is the stable phase at high temperature under small stresses similar to the bulk

Hf_{0.5}Zr_{0.5}O₂. When cooling down, the T phase becomes stable under compressive stress while the M phase is stabilized under tensile stress. Further cooling can stabilize the polar O phase at moderate compressive stress at room temperature. The strain phase diagram gives the range of applied strains to stabilize the polar O phase at room temperature. It is predicted that a moderate compressive strain favors the single O phase which qualitatively agrees with the trend reported in experiments of Hf_{0.5}Zr_{0.5}O₂ epitaxial films grown on perovskite oxide substrates⁴⁰. Moreover, Fig. 4D shows O-T phase coexistence over a wide range of temperatures on the compressively strained side, which agrees well with the experimental observation of strong first-order behavior with a huge thermal hysteresis in Hf_{0.5}Zr_{0.5}O₂ thin films⁴¹. Although the current model of Hf_{0.5}Zr_{0.5}O₂ does not consider the bi-axial misfit strains and the other domain variants of the polymorphic phases, the calculated phase diagrams predict the trend of thermodynamic stability of the polar O phase of Hf_{0.5}Zr_{0.5}O₂ in reasonable agreement with experiments^{40,41}.

Fig. 4D also exhibits topological features analogous to the temperature-composition phase diagrams of binary solutions. For example, there are two isotherm lines, one at $T \sim 500$ K for the O, M, and T phase equilibrium and one at $T \sim 1200$ K for the T, C, and M phase equilibrium. The O-M-T isotherm is eutectic-like while the T-C-M isotherm is peritectic-like. The upper and lower critical points for the O-T and T-C phase equilibria resemble the congruent melting point in binary alloys such as Ni-Ti⁴². The polar O phase serves as an intermediate phase between the nonpolar T and M phases, which is akin to the ordered intermetallic phase in binary alloys such as Mg-Al⁴².

4. Discussion

The thermodynamic theory of strain phase equilibria proposed in this work is generally applicable to multiphase solid-state systems. The proposed thermodynamic framework provides a simple procedure to establish multiphase/multidomain phase diagrams under incoherent conditions by utilizing the corresponding relations between strain and stress phase diagrams. Despite infinitesimal strain and Euler stress tensors are assumed in the present work, the proposed thermodynamic theory with a properly chosen reference state can be applicable to arbitrary conjugated strain-stress pairs (e.g., finite strain tensors⁴³ and symmetry-adapted strain tensors⁴⁴).

It should be mentioned that the strain phase diagrams in this work are obtained assuming incoherent interfaces and negligible interaction between the coexisting phases. The coherent strain

effect may be modeled by including an interaction term in the energy density of the phase mixture (See **Supplementary Note 5 and Fig. S3**). To consider the heterogeneous strains associated with domain walls, homo-/hetero-phase boundaries, surfaces, and other microstructural features generally requires more comprehensive models and numerical simulations such as phase-field modeling⁴⁵. Nevertheless, the strain phase diagrams established by the proposed thermodynamic approach can serve as a first approximation to facilitate the refinement of the strain phase diagrams using other more accurate but computationally much more expensive techniques.

We also would like to point out that there have been extensive theoretical studies revolving around the strain/stress effects on phase equilibria for structural phase transformations by considering the formation of domain and heterophase structures. The earliest exposition on this topic might be attributed to the review article by Roytburd⁴⁶ and the monograph by Khachaturyan⁴⁷. Later on, many thermodynamic models have been proposed^{13,48–50} and phase-field simulations have been performed^{51–53} to establish the strain phase diagrams of ferroelectric/ferroelastic thin films considering the influence of misfit dislocations^{50,54,55}, misfit strain anisotropy^{53,56}, film thickness^{49,54}, domain wall energies^{12,50}, film surface effects⁵⁷, and electrical boundary conditions^{48,52,58}. It is beyond the scope of the present work to survey the literature and give an exposition to all the previous studies. Nevertheless, we highlight that the theoretical framework proposed here differs from most previous works in the incoherent interface assumption, which enables a convenient way to construct the strain phase diagrams without resorting to the specific geometry at the heterophase/domain boundaries. It should be emphasized that essentially all existing temperature-composition chemical phase diagrams are obtained for incoherent conditions.

5. Summary

We develop a general thermodynamic theory for strain phase equilibria and a general thermodynamic framework to efficiently establish strain/stress phase diagrams of solids containing multiphases with structural differences without *a priori* assumptions on the multi-phase/multi-domain coexistence. The minimal required inputs are the free energy density as a function of strain which can be obtained by experiments, first-principles-based simulations, phenomenological thermodynamic models, or by simply assuming linear elasticity theory. We applied the theory to

three exemplary solid-state transformation materials with distinct physics (PbTiO₃, VO₂ and Hf_{0.5}Zr_{0.5}O₂). The strain/stress phase diagrams can be utilized to guide the strain engineering of exotic emergent materials subject to complex deformation, such as twisted multilayers⁵⁹. Moreover, they can also be employed as guide maps to dramatically reduce the number of expensive simulations such as phase-field modeling⁴⁵ for further refining the corresponding strain phase diagrams by taking into account of inhomogeneous microstructures through including thermodynamic energy contributions arising from the domain wall energy and long-range elastic and electrostatic interactions. We expect that our proposed strain equilibria theory and the general framework for constructing strain phase diagrams of strained solids will be broadly applied to guide the exploration of solid-state materials at nanoscale.

Acknowledgment

The work is supported by the National Science Foundation (NSF) through Grant No. DMR-2133373. B. W. is thankful for Dr. Yin Shi in fruitful discussion on the thermodynamic model of VO₂. Part of this work was performed under the auspices of the U.S. Department of Energy by Lawrence Livermore National Laboratory under Contract DE-AC52-07NA27344 (B.W.).

References

- 1. Li, J., Shan, Z. & Ma, E. Elastic strain engineering for unprecedented materials properties. *MRS Bull.* **39**, 108–114 (2014).
- 2. Lee, M. L., Fitzgerald, E. A., Bulsara, M. T., Currie, M. T. & Lochtefeld, A. Strained Si, SiGe, and Ge channels for high-mobility metal-oxide-semiconductor field-effect transistors. *J. Appl. Phys.* **97**, 011101 (2005).
- 3. Schlom, D. G. *et al.* Strain Tuning of Ferroelectric Thin Films. *Annu. Rev. Mater. Res.* **37**, 589–626 (2007).
- 4. Nicholson, C. W. *et al.* Uniaxial strain-induced phase transition in the 2D topological semimetal IrTe2. *Commun. Mater.* **2**, 1–8 (2021).
- 5. Higo, T. *et al.* Perpendicular full switching of chiral antiferromagnetic order by current. *Nature* **607**, 474–479 (2022).
- 6. Ahadi, K. *et al.* Enhancing superconductivity in SrTiO ³ films with strain. *Sci. Adv.* **5**, eaaw0120 (2019).
- 7. Hicks, C. W. *et al.* Strong Increase of T_c of Sr $_2$ RuO $_4$ Under Both Tensile and Compressive Strain. *Science* **344**, 283–285 (2014).
- 8. Ruf, J. P. et al. Strain-stabilized superconductivity. Nat. Commun. 12, 59 (2021).
- 9. Park, J. H. *et al.* Measurement of a solid-state triple point at the metal-insulator transition in VO2. *Nature* **500**, 431–434 (2013).
- 10. Larche, F. C. & Cahn, J. W. Thermochemical equilibrium of multiphase solids under stress. *Acta Metall.* **26**, 1579–1589 (1978).

- 11. Pertsev, N. A. & Koukhar, V. G. Polarization Instability in Polydomain Ferroelectric Epitaxial Thin Films and the Formation of Heterophase Structures. *Phys. Rev. Lett.* **84**, 3722–3725 (2000).
- 12. Roytburd, A. L., Ouyang, J. & Artemev, A. Polydomain structures in ferroelectric and ferroelastic epitaxial films. *J. Phys. Condens. Matter* **29**, 163001 (2017).
- 13. Pertsev, N. A., Zembilgotov, A. G. & Tagantsev, A. K. Effect of Mechanical Boundary Conditions on Phase Diagrams of Epitaxial Ferroelectric Thin Films. *Phys. Rev. Lett.* 80, 1988–1991 (1998).
- 14. Angsten, T. & Asta, M. Epitaxial phase diagrams of SrTiO 3 , CaTiO 3 , and SrHfO 3 : Computational investigation including the role of antiferrodistortive and A -site displacement modes. *Phys. Rev. B* **97**, 134103 (2018).
- 15. Diéguez, O., Rabe, K. M. & Vanderbilt, D. First-principles study of epitaxial strain in perovskites. *Phys. Rev. B* **72**, 144101 (2005).
- 16. Grünebohm, A., Marathe, M. & Ederer, C. *Ab initio* phase diagram of BaTiO ₃ under epitaxial strain revisited. *Appl. Phys. Lett.* **107**, 102901 (2015).
- 17. Chen, L.-Q. Phase-Field Method of Phase Transitions/Domain Structures in Ferroelectric Thin Films: A Review. *J. Am. Ceram. Soc.* **91**, 1835–1844 (2008).
- 18. Hong, S. S. *et al.* Extreme tensile strain states in La _{0.7} Ca _{0.3} MnO ₃ membranes. *Science* **368**, 71–76 (2020).
- 19. Pesquera, D. *et al.* Beyond Substrates: Strain Engineering of Ferroelectric Membranes. *Adv. Mater.* **32**, 2003780 (2020).
- 20. Cui, H. *et al.* Design and printing of proprioceptive three-dimensional architected robotic metamaterials. *Science* **376**, 1287–1293 (2022).

- 21. Wu, P.-C. *et al.* Twisted oxide lateral homostructures with conjunction tunability. *Nat. Commun.* **13**, 2565 (2022).
- 22. Dong, G. *et al.* Super-elastic ferroelectric single-crystal membrane with continuous electric dipole rotation. *Science* **366**, 475–479 (2019).
- 23. Ko, D. L. *et al.* Mechanically controllable nonlinear dielectrics. *Sci. Adv.* **6**, eaaz3180 (2020).
- 24. Elangovan, H. *et al.* Giant Superelastic Piezoelectricity in Flexible Ferroelectric BaTiO ³ Membranes. *ACS Nano* **14**, 5053–5060 (2020).
- 25. Chen, L.-Q. Thermodynamic Equilibrium and Stability of Materials. (2022).
- 26. Chen, L.-Q. & Zhao, Y. From classical thermodynamics to phase-field method. *Prog. Mater. Sci.* **124**, 100868 (2022).
- 27. Hillert, M. *Phase Equilibria, Phase Diagrams and Phase Transformations: Their Thermodynamic Basis.* (Cambridge University Press, 2007).
- 28. Xue, F., Ji, Y. & Chen, L.-Q. Theory of strain phase separation and strain spinodal: Applications to ferroelastic and ferroelectric systems. *Acta Mater.* **133**, 147–159 (2017).
- 29. Sun, W. & Powell-Palm, M. J. Generalized Gibbs' Phase Rule. *ArXiv210501337 Cond-Mat Physicsmath-Ph* (2021).
- 30. Sun, W. & Powell-Palm, M. J. Generalized Gibbs' Phase Rule. 17.
- 31. Kavle, P. *et al.* Strain-Driven Mixed-Phase Domain Architectures and Topological Transitions in Pb1–xSrxTiO3 Thin Films. *Adv. Mater.* **n/a**, 2203469.

- 32. Levanyuk, A. P., Minyukov, S. A. & Misirlioglu, I. B. Loss of elastic stability and formation of inhomogeneous states at phase transitions in thin films on substrates. *Ferroelectrics* **533**, 1–9 (2018).
- 33. Dove, M. T. Theory of displacive phase transitions in minerals. *Am. Mineral.* **82**, 213–244 (1997).
- 34. Levanyuk, A. P., Minyukov, S. A., Burc Misirlioglu, I. & Baris Okatan, M. Effects of interphase boundaries in Ginzburg–Landau one-dimensional model of two-phase states in clamped systems. *J. Appl. Phys.* **129**, 044102 (2021).
- 35. Schofield, P. *et al.* Harnessing the Metal—Insulator Transition of VO2 in Neuromorphic Computing. *Adv. Mater.* 2205294 (2022).
- 36. Shi, Y., Xue, F. & Chen, L.-Q. Ginzburg-Landau theory of metal-insulator transition in VO 2: The electronic degrees of freedom. *EPL Europhys. Lett.* **120**, 46003 (2017).
- 37. Schroeder, U., Park, M. H., Mikolajick, T. & Hwang, C. S. The fundamentals and applications of ferroelectric HfO2. *Nat. Rev. Mater.* (2022) doi:10.1038/s41578-022-00431-2.
- 38. Materlik, R., Künneth, C. & Kersch, A. The origin of ferroelectricity in Hf $_{1-x}$ Zr $_x$ O $_2$: A computational investigation and a surface energy model. *J. Appl. Phys.* **117**, 134109 (2015).
- 39. Batra, R., Tran, H. D. & Ramprasad, R. Stabilization of metastable phases in hafnia owing to surface energy effects. *Appl. Phys. Lett.* **108**, 172902 (2016).
- 40. Estandía, S. *et al.* Engineering Ferroelectric Hf _{0.5} Zr _{0.5} O ₂ Thin Films by Epitaxial Stress. *ACS Appl. Electron. Mater.* **1**, 1449–1457 (2019).

- 41. Mimura, T., Shimizu, T., Sakata, O. & Funakubo, H. Large thermal hysteresis of ferroelectric transition in HfO ₂ -based ferroelectric films. *Appl. Phys. Lett.* **118**, 112903 (2021).
- 42. Okamoto, H. & Okamoto, H. *Phase Diagrams for Binary Alloys*. vol. 44 (ASM international Materials Park, OH, 2000).
- 43. McLellan, A. G. *The Classical Thermodynamics of Deformable Materials*. (Cambridge University Press, 1980).
- 44. Thomas, J. C., Natarajan, A. R. & Van der Ven, A. Comparing crystal structures with symmetry and geometry. *Npj Comput. Mater.* **7**, 1–11 (2021).
- 45. Wang, J.-J., Wang, B. & Chen, L.-Q. Understanding, Predicting, and Designing Ferroelectric Domain Structures and Switching Guided by the Phase-Field Method. *Annu. Rev. Mater. Res.* **49**, 127–152 (2019).
- 46. Roytburd, A. L. The theory of the formation of a heterophase structure in phase transformations in solids. *Sov. Phys. Uspekhi* **17**, (1974).
- 47. Khachaturian, A. Theory of structural transformations in solids. (1983).
- 48. Bratkovsky, A. M. & Levanyuk, A. P. Effects of anisotropic elasticity in the problem of domain formation and stability of monodomain state in ferroelectric films. *Phys. Rev. B* **84**, 045401 (2011).
- 49. Qiu, Q. Y., Nagarajan, V. & Alpay, S. P. Film thickness versus misfit strain phase diagrams for epitaxial PbTiO3 ultrathin ferroelectric films. *Phys. Rev. B* **78**, 064117 (2008).
- 50. Alpay, S. P. & Roytburd, A. L. Thermodynamics of polydomain heterostructures. III. Domain stability map. *J. Appl. Phys.* **83**, 4714–4723 (1998).

- 51. Li, Y. L., Hu, S. Y., Liu, Z. K. & Chen, L. Q. Effect of substrate constraint on the stability and evolution of ferroelectric domain structures in thin films. *Acta Mater.* **50**, 395–411 (2002).
- 52. Li, Y. L., Hu, S. Y., Liu, Z. K. & Chen, L. Q. Effect of electrical boundary conditions on ferroelectric domain structures in thin films. *Appl. Phys. Lett.* **81**, 427–429 (2002).
- 53. Sheng, G. *et al.* Domain stability of PbTiO3 thin films under anisotropic misfit strains: Phase-field simulations. *J. Appl. Phys.* **104**, 054105 (2008).
- 54. Sheng, G. *et al.* Phase-field simulations of thickness-dependent domain stability in PbTiO3 thin films. *Acta Mater.* **60**, 3296–3301 (2012).
- 55. Pompe, W., Gong, X., Suo, Z. & Speck, J. S. Elastic energy release due to domain formation in the strained epitaxy of ferroelectric and ferroelastic films. *J. Appl. Phys.* **74**, 6012–6019 (1993).
- 56. Qiu, Q., Alpay, S. P. & Valanoor, N. Phase diagrams, dielectric response, and piezoelectric properties of epitaxial ultrathin (001) lead zirconate titanate films under anisotropic misfit strains. *J. Appl. Phys.* **107**, 114105–114105 (2010).
- 57. Ma, D. C., Zheng, Y. & Woo, C. H. Surface and size effects on phase diagrams of ferroelectric thin films. *Appl. Phys. Lett.* **95**, 262901 (2009).
- 58. Pertsev, N. A. & Kohlstedt, H. Elastic Stabilization of a Single-Domain Ferroelectric State in Nanoscale Capacitors and Tunnel Junctions. *Phys. Rev. Lett.* **98**, 257603 (2007).
- 59. Sánchez-Santolino, G. *et al.* A 2D ferroelectric vortex pattern in twisted BaTiO3 freestanding layers. *Nature* **626**, 529–534 (2024).

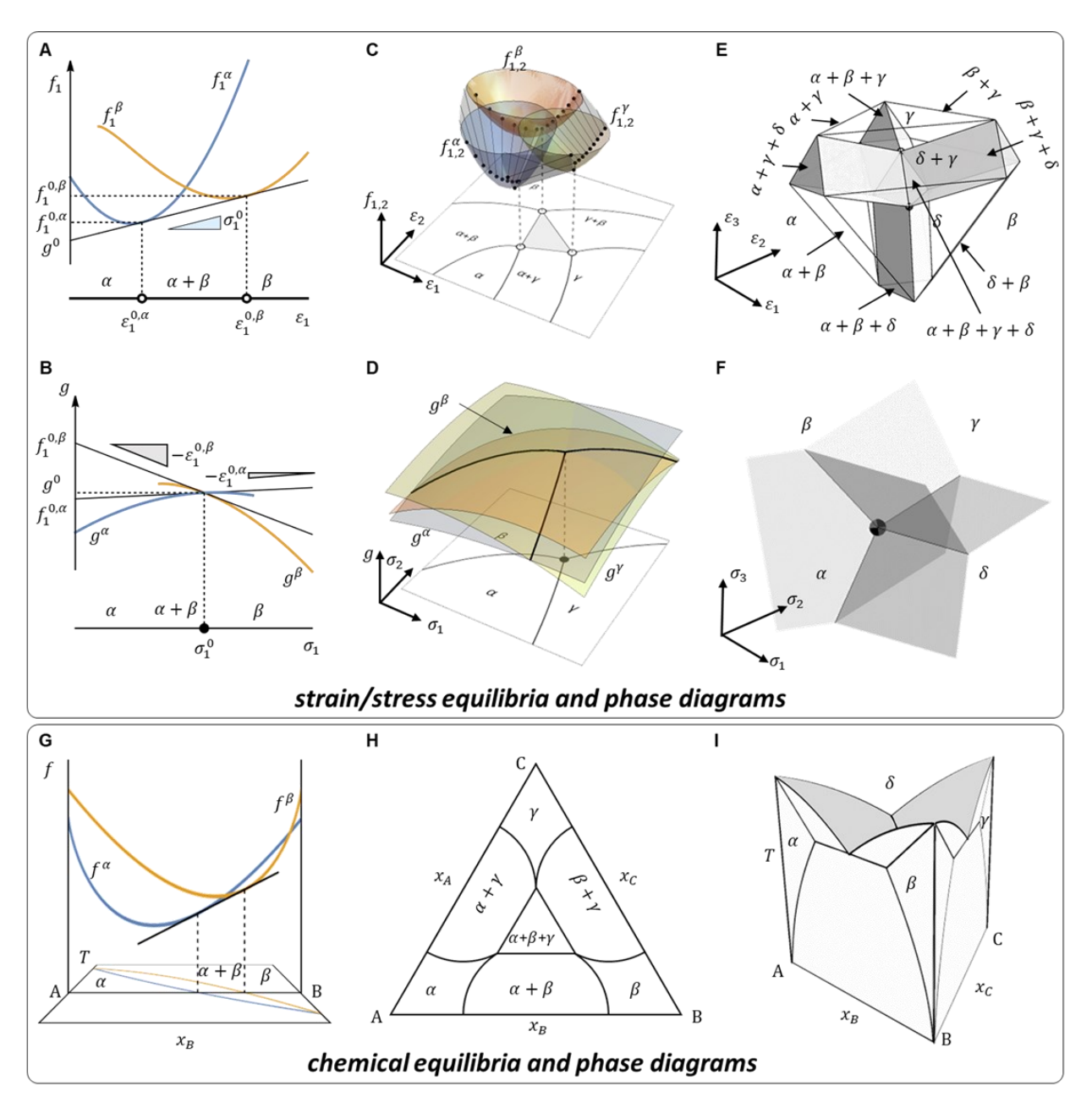


Fig. 1 | Schematics of strain phase diagrams and analogy to chemical phase diagrams. (A – F) Schematics for the construction of (A, C, E) strain and (B, D, F) stress phase diagrams of multiphase/domain solid materials subject to (A, B) one-, (B, D) two-, and (E, F) three-component strains/stresses. α , β , γ , and δ , denote different strain phases/domains in the strain/stress phase diagrams. The solid black dots in (B), (D), and (F) represent the double, triple, and quadruple points for the corresponding stress phase diagrams, respectively. (G – I) Schematics of (G) the construction of a temperature-composition phase diagram of a binary system, (H) an isothermal phase diagram of a ternary system, and (I) a temperature-composition eutectic phase diagram of a ternary system.

Table 1 | Generalized rules and topological features of strain/stress phase diagrams for multiphase/multidomain solid-state materials subject to arbitrary number of strain components.

| Number of strain components | One-component | Two-component | Three-component | n-component |
|---|--|---|--|---|
| # of independent strain variables | 1 | 2 | 3 | n |
| # of independent stress variables | 5 | 4 | 3 | 6 - n |
| common tangent elements | segment | triangle | tetrahedron | n-D simplex |
| degree of freedom (at constant temperature) | 2 - n _p | 3 - n _p | 4 - n _p | n+1 - n _p |
| generalized lever rule* | $\alpha \xrightarrow{L_2 L_1} \beta$ | $\gamma = A_1 A_3 \beta$ α | V_1 δ V_2 γ | n-D simplices |
| | $\frac{\omega_{\alpha}}{\omega_{\beta}} = \frac{L_2}{L_1}$ | $\omega_{\alpha} \colon \omega_{\beta} \colon \omega_{\gamma}$ = $A_1 \colon A_2 \colon A_3$ | $\omega_{\alpha} : \omega_{\beta} : \omega_{\gamma} : \omega_{\delta}$ = $V_1 : V_2 : V_3 : V_4$ | $\omega_{\alpha} \colon \omega_{\beta} \colon \omega_{\gamma} \colon \dots$ = $\tilde{V}_1 \colon \tilde{V}_2 \colon \tilde{V}_3 \colon \dots$ |
| of <i>m</i> -phase regions $N_1, N_2, \dots N_m$ | $N_1 = 2, N_2 = 1$ | $N_1 = 3$, $N_2 = 3$, $N_3 = 1$ | $N_1 = 4$, $N_2 = 6$, $N_3 = 4$, $N_4 = 1$ | $N_m = \binom{n+1}{m}$ |

^{*} The symbols L_1 and L_2 refer to the lengths of the segments, A_1 , A_2 and A_3 refer to the area of the triangles, V_1 , V_2 , V_3 and V_4 refer to the volume of the tetrahedra, and \tilde{V}_i refer to the hypervolume of the *i*-th n-D simplice.

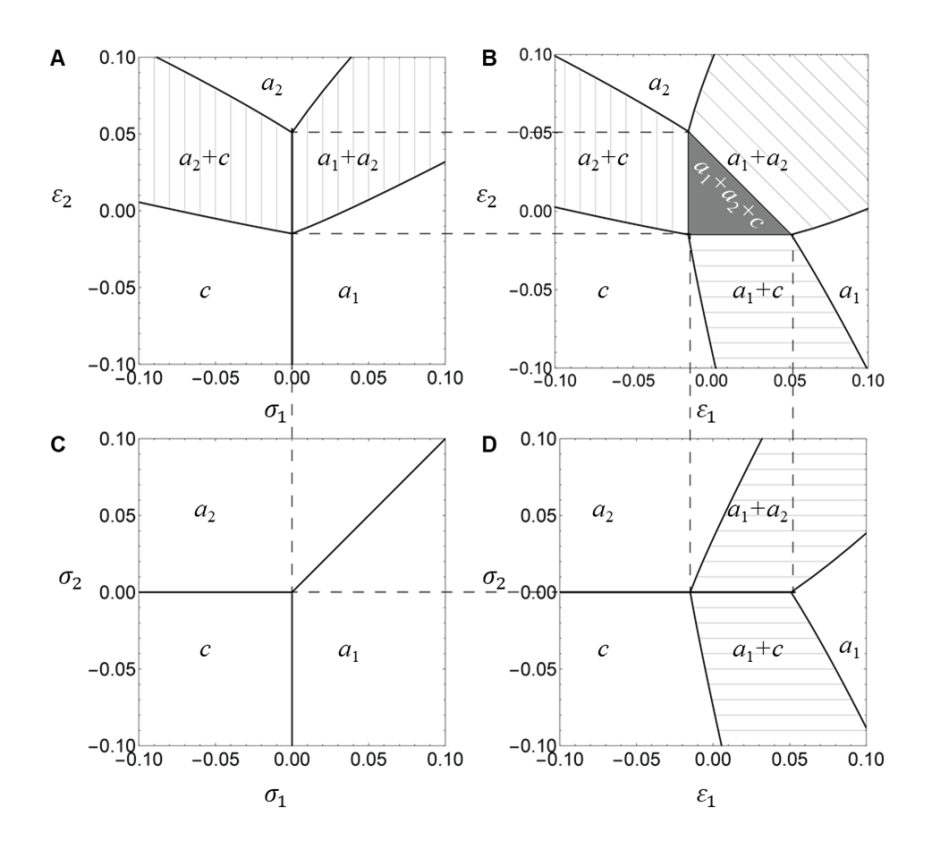


Fig. 2 | Calculated stress-stress, strain-strain, and mixed-type strain-stress phase diagrams of PbTiO₃ subject to two-component normal strains at 300 K. In each subfigure, the thick lines are phase boundaries, and the thin lines are the tie-lines of the two-phase regions. The dashed lines connecting the subfigures suggest the corresponding relations between the three-phase regions in each phase diagram. The unit of all the stress components is GPa.

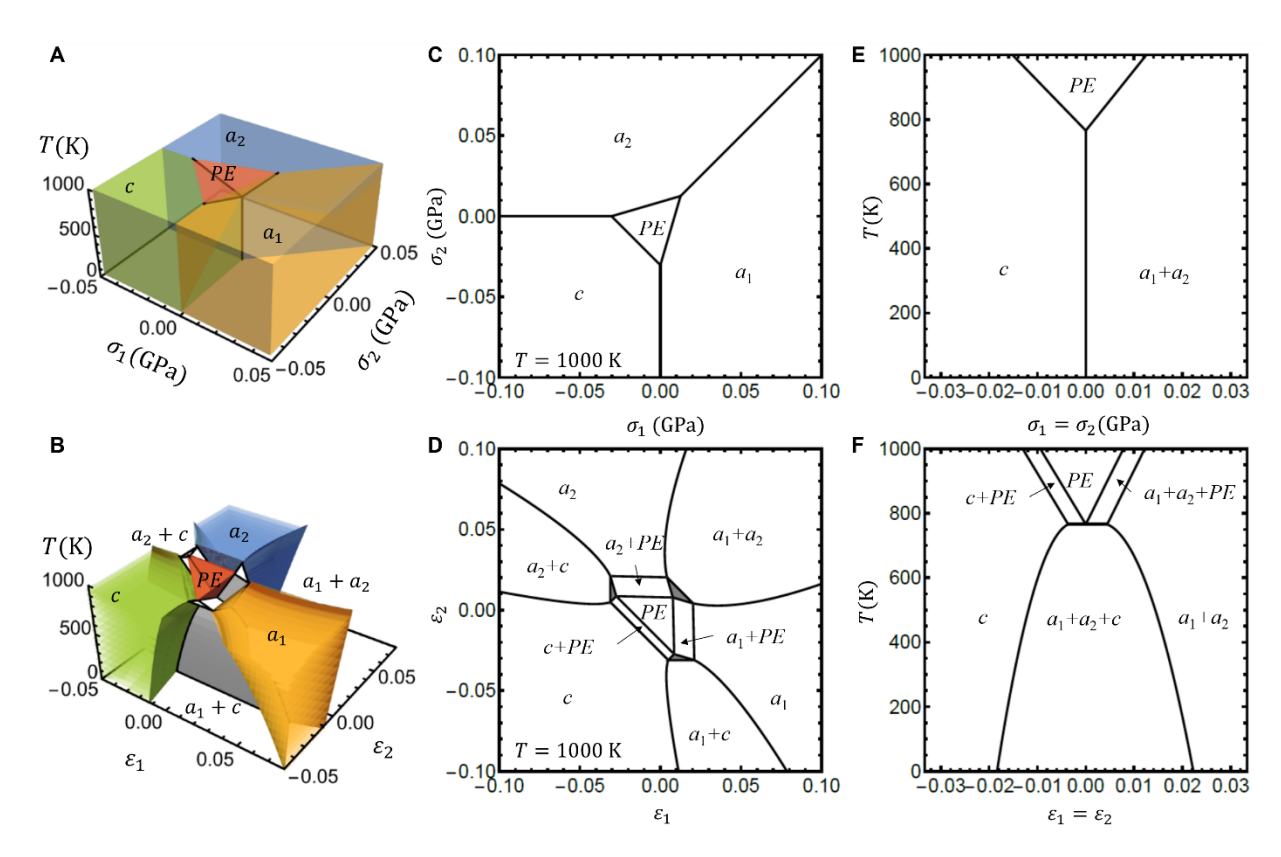


Fig. 3 | Calculated 3-D temperature-strain and temperature-stress phase diagrams of biaxially strained PbTiO₃ and their cross sections. (A) The temperature-stress-stress phase diagram. (B) The temperature-strain-strain phase diagrams. (C) The isothermal stress-stress phase diagram at T = 1000 K. (D) The isothermal strain-strain phase diagram at T = 1000K. (E) The temperature-stress for equi-biaxial 2-D stress with $\sigma_1 = \sigma_2$. (F) The temperature-strain for equi-biaxial 2-D strain with $\varepsilon_1 = \varepsilon_2$.

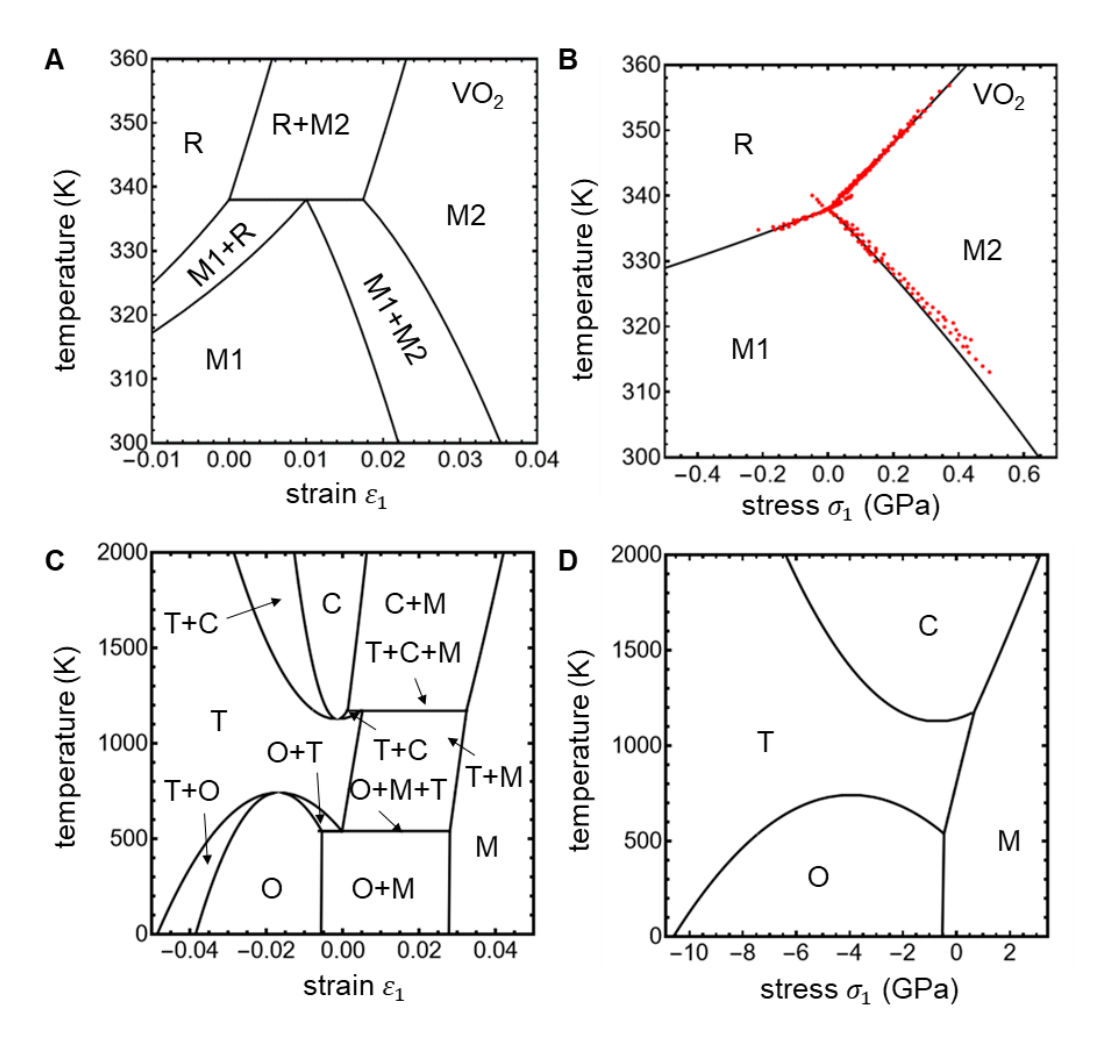


Fig. 4 | Calculated strain and stress phase diagrams of solid-state materials undergoing structural phase transformations. (A) The temperature-strain and (B) temperature-stress phase diagrams of VO₂ subject to uniaxial normal strain/stress. The two monoclinic phases are denoted as M1 and M2 and the rutile phase is denoted as R. The red dots in (B) are experimental measurements adopted from Ref. ⁹. (C) The temperature-strain and (D) temperature-stress phase diagrams of 20 nm Hf_{0.5}Zr_{0.5}O₂ epitaxial thin film subject to uniaxial normal strain/stress. The cubic, tetragonal, polar orthorhombic, and monoclinic phases are denoted as C, T, O, and M respectively.